Nuclear Instruments and Methods in Physics Research A 387 (1997) 377–394

NUCLEAR INSTRUMENTS & METHODS IN PHYSICS RESEARCH Section A

ELSEVIER

A 3000 element lead-glass electromagnetic calorimeter

R.R. Crittenden[a], A.R. Dzierba[a], J. Gunter[a], R. Lindenbusch[a], D.R. Rust[a], E. Scott[a], P.T. Smith[a], T. Sulanke[a], S. Teige[a], B.B. Brabson[a,*], T. Adams[b], J.M. Bishop[b], N.M. Cason[b], J.M. LoSecco[b], J.J. Manak[b], A.H. Sanjari[b], W.D. Shephard[b], D.L. Steinike[b], S.A. Taegar[b], D.R. Thompson[b], S.U. Chung[c], R.W. Hackenburg[c], C. Olchanski[c], D.P. Weygand[c], H.J. Willutzki[c], S. Denisov[d], A. Dushkin[d], V. Kochetkov[d], V. Lipaev[d], A. Popov[d], I. Shein[d], A. Soldatov[d], Z. Bar-Yam[e], J.P. Cummings[e], J.P. Dowd[e], P. Eugenio[e], M. Hayek[e], W. Kern[e], E. King[e], E.V. Anoshina[f], V.A. Bodyagin[f], A.I. Demianov[f], A.M. Gribushin[f], O.L. Kodolova[f], V.L. Korotkikh[f], M.A. Kostin[f], A.I. Ostrovidov[f], L.I. Sarycheva[f], N.B. Sinev[f], I.N. Vardanyan[f], A.A. Yershov[f], D.S. Brown[g], T.K. Pedlar[g], K.K. Seth[g], J. Wise[g], D. Zhao[g], G.S. Adams[h], J. Napolitano[h], M. Nozar[h], J.A. Smith[h], M. Witkowski[h]

[a] *Department of Physics, Indiana University, Bloomington, IN 47405, USA*
[b] *Department of Physics, University of Notre Dame, Notre Dame, IN 46556, USA*
[c] *Department of Physics, Brookhaven National Laboratory, Upton, L.I., NY 11973, USA*
[d] *Institute for High Energy Physics, Protvino, Russian Federation*
[e] *Department of Physics, University of Massachusetts Dartmouth, North Dartmouth, MA 02747, USA*
[f] *Institute for Nuclear Physics, Moscow State University, Moscow, Russian Federation*
[g] *Department of Physics, Northwestern University, Evanston, IL 60208, USA*
[h] *Department of Physics, Rensselaer Polytechnic Institute, Troy, NY 12180, USA*

Received 1 July 1996; revised form received 29 September 1996

Abstract

A 3045 element lead glass calorimeter and an associated fast trigger processor have been constructed, tested and implemented in BNL experiment E852 in conjunction with the multi-particle spectrometer (MPS). Approximately, 10^9 all-neutral and neutral plus charged triggers were recorded with this apparatus during data runs in 1994 and 1995. This paper reports on the construction, testing and performance of this lead glass calorimeter and the associated trigger processor.

Keywords: Calorimeter; Lead glass; Trigger processor

1. Introduction

Brookhaven AGS experiment E852, a search for mesons with unusual quantum numbers, used the multiparticle spectrometer (MPS) [1] with several major additions. Fig. 1 shows the experimental layout including these upgrades. In the target region the upgrades included a cesium iodide barrel [2] to provide a soft photon veto and a 4 layer cylindrical drift/proportional chamber for charged particle tracking and triggering [3]. In the downstream region behind the MPS magnet, a new 3.5 m × 2.5 m drift chamber and the 3045 element lead glass detector (LGD) were added. Between the target and the LGD we added a charged particle veto wall used in all-neutral triggers, and a picture frame lead-scintillator sandwich countersystem to veto photons outside of the region of the lead glass detector.

The experiment was designed to run several triggers simultaneously, including all-neutral and all-charged triggers, as well as triggers with both charged and neutral

* Corresponding author. Tel.: + 1 812 855 3881; fax: + 1 812 844 0440; e-mail: brabson@indiana.edu

PII S0168-9002(97)00101-0

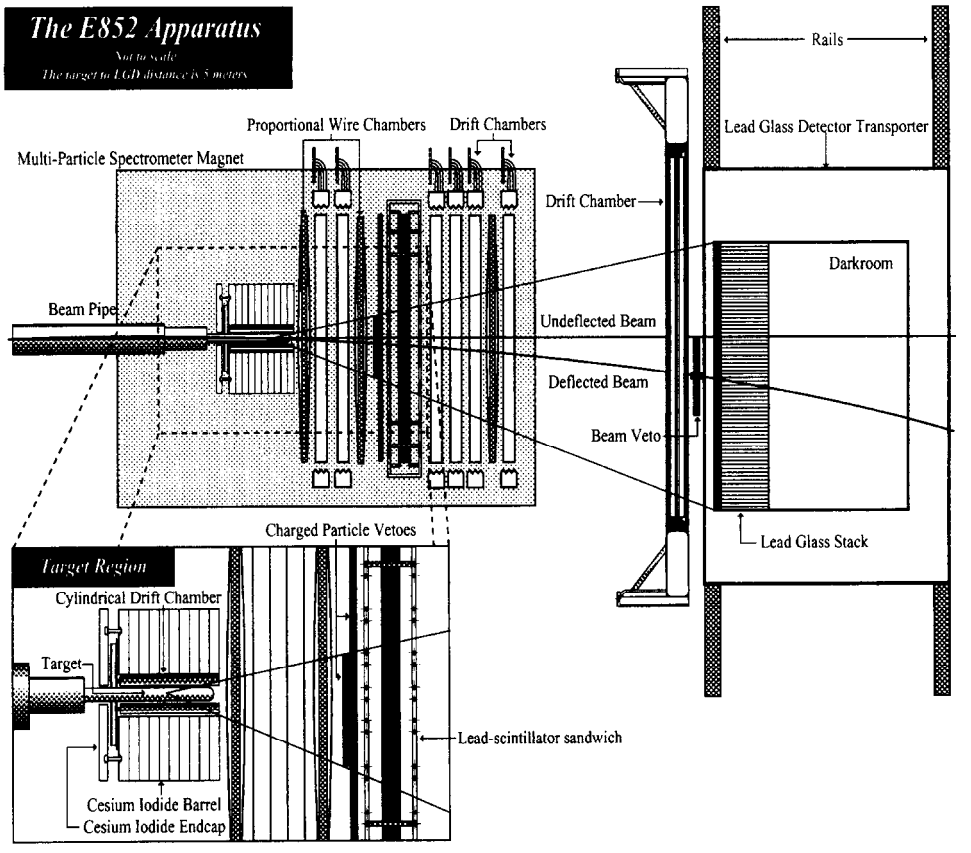

Fig. 1. Plan view of Experiment E852.

particles. A new data acquisition system was implemented to allow us to handle the high data rates produced by the multiple triggers.

This paper focuses on the design, construction, and performance of the lead glass detector. A previous publication [4] describes two prototypes for this detector and provides references to other lead-glass calorimeter systems [5]. The performance characteristics of the detector are determined from physics runs in 1994 (May – July) and 1995 (January – June). During these periods a total of approximately 10^9 events were recorded with LGD information.

The LGD system includes the 9 ton glass array of 4 cm × 4 cm × 45 cm blocks, a transporter capable of placing each module in an electron beam for calibration and a monitoring system. Section 2 of this paper describes the full mechanical construction of the LGD system, including the transporter and the monitoring system. Section 3 describes the LGD electronics for data collection, readout, and triggering. A unique feature of E852 is the ability to make a trigger decision based on either the total energy or the effective mass of a system of photons. A hardware trigger processor, making use of custom built ADCs [4], uses the distribution of energy in the LGD to approximate the overall neutral energy effective mass [6]. We enhanced η's in our triggers, for example, by requiring an effective mass greater than the mass of the π^0.

Section 4 of this paper describes optical coupling and magnetic shielding tests of the LGD system. Constrained fitting of photons from π^0's and η's provides a calibration technique described in Section 5 of the paper. Section 6 describes the energy monitoring carried out during the data collection periods. Finally, Section 7 addresses the performance of the LGD during recent physics runs.

2. Lead-glass detector mechanical design

2.1. Calorimeter components

The lead-glass detector (LGD) consists of an array of 3045 4 cm × 4 cm × 45 cm type F8-00 lead glass blocks stacked in a 43 × 71 rectangle (four corner blocks and four central blocks were removed). Cherenkov light

produced by interacting photons and electrons is measured by type FEU-84-3 Russian made photomultipliers. High voltage for the photomultipliers was supplied by computer-controlled, Cockcroft–Walton-type bases. The tube/base assemblies are held in an aluminum and soft iron structure referred to below as the cellular wall. The entire assembly is carried by a transporter to allow each module to be placed in an electron beam for calibration. A laser-based monitoring system was used to illuminate the detector. The glass, photomultipliers and bases are described in detail in Ref. [4].

The transverse dimensions of each block were determined by an automated measuring system. The average block size was 40.0068 mm with a standard deviation of 24.0 μm. The high precision machining of the blocks allowed them to be stacked tightly in the array. The space between two typical blocks (as determined by a feeler gauge) was less than 100 μm.

The quantum efficiency and noise rate was measured for each tube. The average quantum efficiency was 21% with a standard deviation of 3%. The Cockcroft–Walton voltage multiplier bases [7] have the advantages of relatively low power use (2 KW for the 3045 bases and power distribution system) and reduced cabling.

2.2. The LGD transporter

We calibrate the lead-glass detector using two different techniques. In the first each lead-glass block is placed in a beam of electrons of known energy. In the second the energies of photons incident on the lead-glass array are determined by using kinematic constraints on known physics processes such as π^0 decays. A transporter was designed and built to accomplish the task of moving the entire lead-glass array, its support frame, magnetic shielding, dark room and a portion of the delay cables. The system was required to move each glass block into the electron beam with an accuracy of $\pm$ 1 mm, and at such a rate that the entire 3045 block array could be calibrated in an electron beam in a few hours.

There are advantages of each calibration technique and cross-checks available when both are used. Among the advantages of placing each lead-glass block in an electron beam of known energy is the ability to reach all blocks in the array with sufficient particles to do a high statistics calibration of each module, even those near the edges of the LGD where few photons are found. A disadvantage of calibrating with relatively low momentum electron beams (3–5 GeV/c) follows from the need to turn off the MPS magnet during calibration. Variations in photomultiplier gain from the fringe field of the MPS magnet are not taken into account in such a calibration.

Calibration with photons from physics processes taking place in the target has several desirable characteristics. The calibrating photons are selected to be similar to those used in the final physics analyses. The angles of incidence, the energies, and the depths of the showers are well represented by these calibration photons.

The transporter system consists of four major components (see Fig. 2). We refer to these components as the inner frame, the outer frame, the drive system and the rails. The inner frame, constructed of welded steel tube, carries the lead glass, the cellular wall (described in Section 2.3), the photomultipliers and their bases and a light-tight enclosure at the rear of the detector. The inner frame can move vertically via the vertical component of the drive system. The inner frame is, in turn, carried by the outer frame. The outer frame has guide rails to constrain the vertical motion of the inner frame and flanges to support the ball screws of the vertical drive system. The wheels of the outer frame rest on the rails to provide horizontal motion. The rails are bolted and grouted to the floor of the experimental hall.

Motion of the transporter is provided by the horizontal and vertical drive systems. Vertical motion is produced by ball screws driven through worm drive speed reducers by a high torque stepping motor. Electrically operated brakes, locked when the power is off, hold the transporter in place vertically. Horizontal motion is produced by a rack and pinion system driven through a worm gear speed reducer. An identical high torque stepping motor drives this horizontal system. The transporter is constrained to its path on the rails by a guide roller system with wheels on the transporter and a guide block on the front rail.

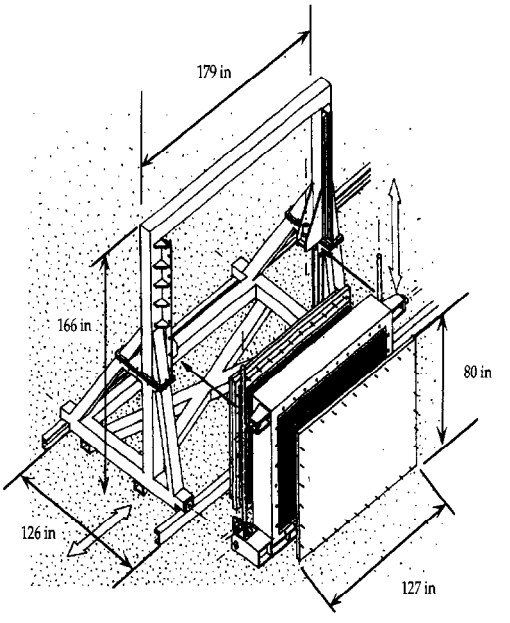

Fig. 2. A schematic of the lead-glass detector and transporter used in Brookhaven Experiment E852.

A torque limiter between the horizontal stepping motor and the speed reducer mechanically disconnects the motor in the event the transporter encounters an obstacle to horizontal motion. Limit switches and an interlock system prevent motion outside the desired range and operation of the system during periods when safety considerations forbid it.

The transporter position is determined by rotational position transducers connected to the speed reducers. A comparison of mechanical position measurements and the position measurements derived from these transducers shows that the transducers produce repeatable results that agree with the independent mechanical measurement to within $\pm$ 1.0 mm. Table 1 summarizes some of the parameters of the horizontal and vertical drive systems. Further detail on the motor drive system, the interlocks, and the rotational position transducers is given in Ref. [4].

The transporter was fabricated, assembled, and mounted on a rail system in the high bay area of the Indiana University Physics Department. There, safety tests of the transporter were conducted by exercising the full range of motion of the transporter under load. The transporter functioned properly while bearing a dead weight of 16 800 kg, corresponding to 125% of expected load.

2.3. The cellular wall

An aluminum and soft iron assembly was constructed to hold the photomultiplier/base assemblies at the rear of the lead glass blocks. This cellular wall served two purposes: *first*, mechanical support and alignment of the photomultipliers and their bases and *second*, magnetic shielding of the tubes. The design selected to achieve these goals consisted of a sandwich of two aluminum plates supporting soft iron tubes between them. The two aluminum plates, each 1.27 cm thick, had 3053 (43 vertical by 71 horizontal) holes. The holes were $3.9497^{+0.0025}_{-0.0000}$ cm in diameter on 4.0008 $\pm$ 0.0051 cm centers, leaving only 0.0584 cm of aluminum stock between holes. Each hole in one of the plates received a press fit machined soft iron tube. When all the tubes were installed, the second plate was placed atop the array of tubes. The tubes were machined to have a slip fit into the upper plate. The outer edges of the plates were secured to aluminum blocks to provide a structure rigid enough to be moved. Further rigidity was obtained by filling the inter-tube gaps with epoxy. The epoxy (215 l) was pumped in under pressure in stages, and was allowed to cure between stages. Low viscosity epoxy [8] was selected for this purpose. Three layers of μ-metal (total of 300 μm) installed in the front half of each soft iron tube provided added magnetic shielding.

The effectiveness of this magnetic shielding was tested under actual operating conditions at the MPS during our June–July 1993 engineering run, and is discussed in Section 4.1.

Table 1
Summary of parameters of the lead-glass detector transporter drive system

Variable	Vertical	Horizontal
Velocity (cm/min)	15.2	61.0
Motor step rate (steps/s)	3200	4775
Step mode[a] (steps/rev)	200	1000
Motor speed (rev/s)	16	4.775
Full range of travel (cm)[steps]	173[2,176,000]	732[6,878,000]
Acceleration/deceleration ramps (s)	1	1
Required motor torque (N cm)	700	1343[b]
Available motor torque (N cm)	1768[c]	2687

[a]Full for horizontal and 1/5 for vertical.
[b]Torque required to climb a 1.5 mm obstacle.
[c]At 16 rev/s.

2.4. The darkroom and cabling

Bolted onto the frame holding the lead glass stack and cellular wall is an air-conditioned darkroom structure (see Fig. 3). The darkroom allows the servicing of the photomultipliers and bases without removing voltage from the 3045 PMTs. Entrance into the dark room is through a revolving door. In the darkroom the signal/delay cables from the cellular wall are funneled into Goretube™ [9] cable carriers fastened to the back of the dark room. These 250 ns long cables continue on to the ADCs. In addition to protecting the cables during motion of the transporter, these cable carriers provide rf-shielding. A section of Goretube is visible in Fig. 3.

A cabling algorithm [10] was developed to minimize the read-out time of the ADCs for typical energy deposition in the LGD. The ADCs resided in 4 FASTBUS crates and zero-suppressed read-out was used. Therefore, the read-out time could be minimized by spreading hits out among the four crates and insuring that, within a crate, as few modules as possible had hits. An optimized cable arrangement gained a factor of roughly two in ADC read-out speed compared to a simple sequential mapping of photomultiplier to ADC channel.

2.5. The monitoring system design

Lead-glass systems are often monitored by sending a separate optical fiber to each lead glass module. Such

Fig. 3. The LGD transporter and darkroom.

a system is costly and is mechanically difficult to set up and to maintain with uniformity of illumination from module to module. In an earlier prototype for the present experiment, a cast acrylic bar and nipple system, illuminated by 4 fibers, was used to distribute light to an 18×18 glass block array. The light output varied by a factor of about 2.5 from the corners (where the fibers were attached) to the center, due to attenuation in the acrylic bars [4].

In the present system a pulsed nitrogen laser [11] with an average power of 6 mW, a maximum pulse energy of 400 μJ and a peak emission of 337 nm, excited a small cylinder of scintillator (1.27 cm thick, 2.54 cm diameter) housed inside the laser enclosure. Safety considerations were satisfied by insuring that only scintillator light left this enclosure. The scintillator was viewed by a bundle of optical fibers, 18 of which carried light to the edges of three 99 cm × 175 cm × 1.27 cm acrylic sheets [12] mounted directly in front of the wall of lead glass blocks. Sufficient light was scattered out of the acrylic sheets and onto the photocathodes to give a pulse with an amplitude equivalent to a 7 GeV shower, approximately 1000 ADC counts. An additional four fibers carried light to an RCA8575 photomultiplier tube in the dark room at the same (controlled) temperature as the photomultipliers of the lead-glass wall. In addition, this control tube was magnetically shielded. The signals from this tube were used to measure the pulse to pulse variation of the laser output.

To control the amount of light from the scintillator reaching the optical fiber bundle, the fiber bundle was mounted on an 11″ long optical mini-rail inside the laser cavity. The end of the bundle could be moved along the rail to achieve optimum light intensity, exploiting the fact that the light from the scintillator was emitted isotropically. An aluminum foil mask at the scintillator was also used to reduce the light intensity. The entire laser/fiber bundle assembly was mounted on and moved with the LGD frame. The implementation of the monitoring system is discussed in Section 6 of this paper.

Two tests of this monitoring design are described here. Section 6 describes the performance of the monitoring system during the physics runs of experiment E852. The first test measured the light distribution across the acrylic sheets. By moving a lead-glass/photomultiplier assembly across the surface of a single sheet, the uniformity across the sheet was determined to be within $\pm$ 5%. A second test was carried out during the 1993 engineering run of E852 where 81 blocks of the full 3045 in the lead glass array were instrumented. To look for possible cross-talk effects introduced by the acrylic sheets of the monitoring system (due to light leaving the front face of one block, traveling through the acrylic sheets, and into neighboring blocks) the instrumented region of the glass stack was

positioned in the region of a seam between two acrylic sheets. No evidence of crosstalk through the monitoring system was found.

3. Lead-glass detector electronics design

A unique feature of the lead-glass detector in experiment E852 is the ability to calculate the all-neutral effective mass as part of the trigger requirement. To accomplish this, the neutral energy deposited in the LGD is read out, digitized by fast ADCs, and processed by a fast trigger processor in a total time of approximately 10 μs. The trigger processor is therefore able to handle up to 10^4 events per second at 10% dead time.

An interaction pre-trigger is formed during the first 200 ns after beam crossing. The delay cables between the LGD and the ADCs store the analog information during this period. The ADC integration gate of 250 ns is followed by a 750 ns integrator settling time, and a 3 μs ADC digitization period. The digitized signals are passed on to the fast trigger processor which makes an effective mass decision in typically 5 μs. Here we review the essential features of the ADCs and describe their implementation in the trigger for the 3045 element lead glass array of E852. More detail concerning the ADCs is given in Ref. [4]. The trigger processor is described in Section 3.2.

3.1. Analog-to-digital converters

The ADCs are packaged as FASTBUS modules with 32 channels per module. For each channel the input signal above a pre-sampled baseline is integrated and presented to two discriminators and a successive-approximation 12-bit digitizer. The two discriminators have separate thresholds and their outputs are available 100 ns after the end of integration for use in a first-level trigger (e.g. multiplicity counting). The baseline subtraction feature provides good noise immunity and makes possible the realization of the full dynamic range of the ADC. For example, 60 Hz, 1 V amplitude noise added to the signal produces a shift in the output of less than one least count. These ADC characteristics are summarized in Table 2.

When an ADC module is read out, the ADC value is contained in the 12 lowest-order bits of the 32 bit FASTBUS word. Two bits report the discriminator states. The high-order 16 bits of the FASTBUS word contain a channel identifier. The lower level discriminator is used to select those channels to be read out as part of an event, while the upper level discriminator is used to select those channels to be considered by the trigger processor (see Section 3.2). The discriminator outputs are also available on the module auxiliary connector. These discriminator thresholds can be set by means of two 12 bit DACs. The pedestal for each channel can be trimmed by means of an 8 bit DAC. A 16 bit DAC provides a test voltage. Each channel has a test pulser which injects a charge proportional to this test voltage. The channels participating in this test can be selected by a 32 bit test mask register.

Table 2
Characteristics of the custom-built ADCs.

Number of bits	12
Full-scale charge	1 nC
Digitizing time	3 μs
Number of channels/FASTBUS module	32
Event read-out time for full LGD 4 crates reading in parallel and 4% occupancy	5 μs
Reset time (to 1 bit accuracy)	250 ns
Integral non-linearity	0.025%
Other features:	
Noise rejection	
On-board discriminators	

A full crate of ADC modules can be self-tested by a *broadcast write* to a bit in a register. Several block transfer modes are implemented. The highest speed mode for sparse data is multi-module data transfer (MDT), which allows a full crate of ADC modules to be read with a single FASTBUS block transfer. Once read-out starts, control is automatically passed from module to module without additional FASTBUS addressing cycles.

Special high current supplies [13] provided power to the four ADC crates. In addition, a dedicated air conditioning system delivered cool air directly to the bottom of each FASTBUS crate. Fans located on top of each crate ejected warm air into the room. Temperature sensors monitored the warmed air, and input power was removed from the ADC crates if overheating was detected.

3.2. Trigger processor

The physics goals of experiment E852 required an event trigger on the presence of an η in the final state. Since the η has large branching ratios both into 2γ and into $3\pi^0$, a trigger processor [6] was designed that could quickly evaluate the effective mass of a system of photons. The effective mass squared of n photons is given by

$$m^2 = \left(\sum_{i=1}^{n} E_i\right)^2 - \left(\sum_{i=1}^{n} \boldsymbol{p}_i\right)\cdot\left(\sum_{i=1}^{n} \boldsymbol{p}_i\right). \quad (1)$$

Since a photon deposits its energy over several blocks in the lead glass array, the energy and momentum of the ith photon are determined by summing over a cluster of

blocks in the detector. For example, the energy of the ith photon is

$$E_i = \sum_{j=1}^{l_i} C_j \mathrm{PH}_j \tag{2}$$

where l_i is the number of blocks in the ith cluster, PH_j is the pedestal subtracted pulse height in the jth block and C_j is the calibration constant of the jth block. Similarly, the momentum of the ith photon is

$$\boldsymbol{p}_i = \frac{\boldsymbol{r}_i}{|\boldsymbol{r}_i|} \sum_{j=1}^{l_i} C_j \mathrm{PH}_j. \tag{3}$$

Substituting these expressions into Eq. (1), and using the approximation $|\boldsymbol{r}_i| \approx |\boldsymbol{r}_j|$ within a cluster, the double sums can be replaced with a single sum over all N blocks in the event giving

$$m^2 = \left(\sum_{k=1}^{N} C_k \mathrm{PH}_k\right)^2 - \left(\sum_{k=1}^{N} \frac{C_k \mathrm{PH}_k \boldsymbol{r}_k}{|\boldsymbol{r}_k|}\right) \cdot \left(\sum_{k=1}^{N} \frac{C_k \mathrm{PH}_k \boldsymbol{r}_k}{|\boldsymbol{r}_k|}\right). \tag{4}$$

Expanding the dot product in Eq. (4) gives

$$m^2 = \left(\sum_{k=1}^{N} C_k \mathrm{PH}_k\right)^2 - \left(\sum_{k=1}^{N} \frac{C_k \mathrm{PH}_k x_k}{|\boldsymbol{r}_k|}\right)^2 - \left(\sum_{k=1}^{N} \frac{C_k \mathrm{PH}_k y_k}{|\boldsymbol{r}_k|}\right)^2 - \left(\sum_{k=1}^{N} \frac{C_k \mathrm{PH}_k z_k}{|\boldsymbol{r}_k|}\right)^2. \tag{5}$$

Defining

$$q_{kx} = \frac{C_k x_k}{|\boldsymbol{r}_k|}, \tag{6}$$

$$q_{ky} = \frac{C_k y_k}{|\boldsymbol{r}_k|}, \tag{7}$$

$$q_{kz} = \frac{C_k z_k}{|\boldsymbol{r}_k|}, \tag{8}$$

and substituting into Eq. (5) gives

$$m^2 = \left(\sum_{k=1}^{N} C_k \mathrm{PH}_k\right)^2 - \left(\sum_{k=1}^{N} \mathrm{PH}_k q_{k_x}\right)^2 - \left(\sum_{k=1}^{N} \mathrm{PH}_k q_{k_y}\right)^2 - \left(\sum_{k=1}^{N} \mathrm{PH}_k q_{k_z}\right)^2. \tag{9}$$

As the first and fourth terms of this equation are large and of opposite sign, a rearrangement of the terms in this equation provides greater precision.

$$m^2 \approx 2\left(\sum_{k=1}^{N} C_k \mathrm{PH}_k\right)\left(\sum_{k=1}^{N} \mathrm{PH}_k \delta_{k_x}\right) - \left(\sum_{k=1}^{N} \mathrm{PH}_k q_{k_y}\right)^2 - \left(\sum_{k=1}^{N} \mathrm{PH}_k q_{k_z}\right)^2. \tag{10}$$

Note that the constants, C_k, $\delta_k = C_k - q_{k_3}$ and q_k depend only on the address of a block, and hence on the direction cosines of the block and its calibration constant. The sums in Eq. (10) can be quickly evaluated using commercially available multiply/accumulate circuits. The q_k terms are approximated as integers and down-loaded to the processor. Erasable programmable read-only memory (EPROMs) are used to store these constants.

A by-product of the calculation of the effective mass is the total photon energy calculated in the first sum of Eq. (9). The total photon energy in the LGD is, of course, a powerful selector of well contained all-neutral events and was used as part of the all-neutral trigger.

3.2.1. *Trigger processor read-out controllers*

The E852 LGD read-out controller (see Fig. 4) is a single width FASTBUS module. Each of the 4 crates of LGD ADCs has one such read-out controller. At the request of the trigger processor, the read-out controller reads out the ADCs in its crate, buffers the data in a dual port RAM, and presents the data on ribbon cable to the trigger processor. The dual port RAM has pointers enabling the RAM to act as a FIFO (first-in-first-out). The four crates are read out in parallel.

3.2.2. *Trigger processor logic*

A block diagram of the trigger processor is shown in Fig. 5. During a read-out, sums corresponding to the 4-vector components of Eq. (2) are evaluated as are the largest pulse height and the number of blocks over threshold. The 32-bit ADC word is split into a 12-bit address and the upper 8 bits of data. The address is used to look up the calibration constants (LUCC) stored in the corresponding EPROM's, and the other position dependent constants needed in Eq. (2). These constants are multiplied by the data part of the ADC word and

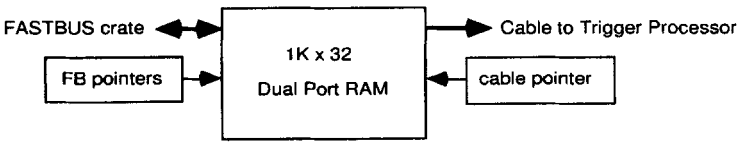

Fig. 4. Read-out controller (ROC) schematic.

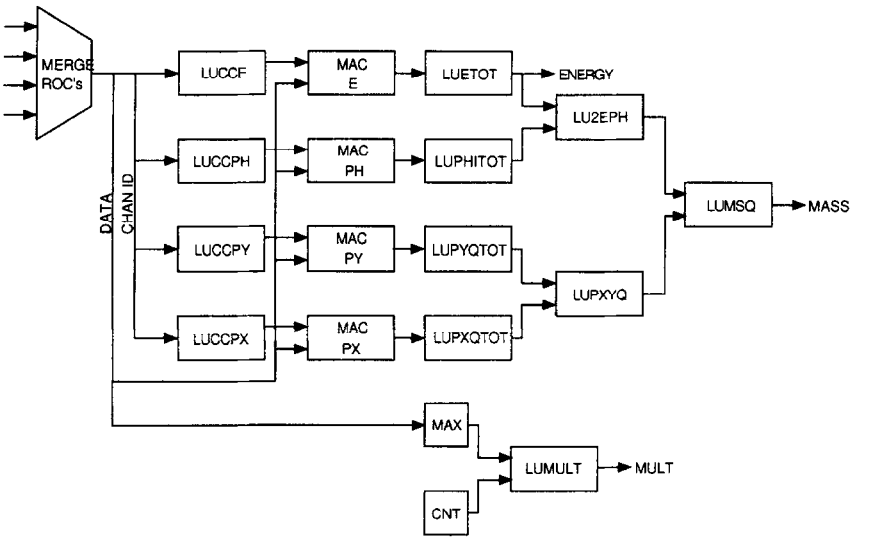

Fig. 5. A block diagram of the trigger processor.

added to a stack by the multiply and accumulate (MAC) circuits.

After read-out is complete, the sums in the MAC stacks are used as addresses in another stage of EPROMs. These EPROMs return functions of the values of the sums from the MACs. For example, the value of P_x^2 is computed from the value of P_x. These function values, in turn, serve as addresses for subsequent EPROMs until the effective mass squared is evaluated. A calculation similar to this one can evaluate the momentum transfer to the photon system.

For diagnostic purposes the data from an event remain in the trigger processor and can be read out through FASTBUS. There is also a self-test mode which assumes the readout controllers have been loaded with test data and had their cable pointers zeroed. This test mode does not read the ADC data. Another possible test mode is to generate test data in the ADC's, read them with the readout controllers, and then to start the trigger processor self-test.

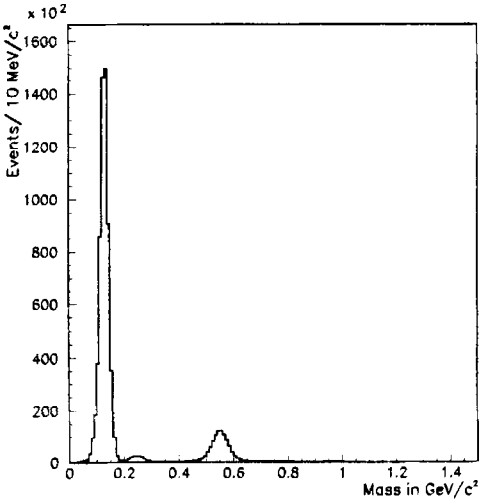

Fig. 6. The two photon effective mass distribution (in GeV/c^2) without a trigger processor requirement.

3.2.3. Trigger processor performance

A measure of the effectiveness of the trigger processor is its effect on the two photon mass spectrum. Figs. 6 and 7 show the effective mass of two photon events with and without a trigger processor requirement. Fig. 6 shows the decays $\pi^0 \to \gamma\gamma$ and $\eta \to \gamma\gamma$ in the ratio of $\approx 20:1$. Fig. 7 shows the observed two-photon effective mass distribution when the trigger processor was configured to select events with a photon system with an effective mass greater than the mass of the π^0.

To enhance the speed of the trigger processor, only the upper 8 bits of the 12-bit ADCs were used as input to fast 8-bit multiply/accumulate chips. Additional speed was achieved by presenting to the trigger processor only ADC channels above a selectable threshold. As described above, the custom-built ADCs have two discriminators on each channel. One was set to a low threshold to select channels that were read by the data acquisition system. The second higher threshold selected channels presented to the trigger processor. The effective mass resolution of the trigger processor is approximately 5%. This resolution allowed us to set the trigger processor threshold just above the π^0 mass peak, and far enough below the η mass, to avoid an η trigger bias.

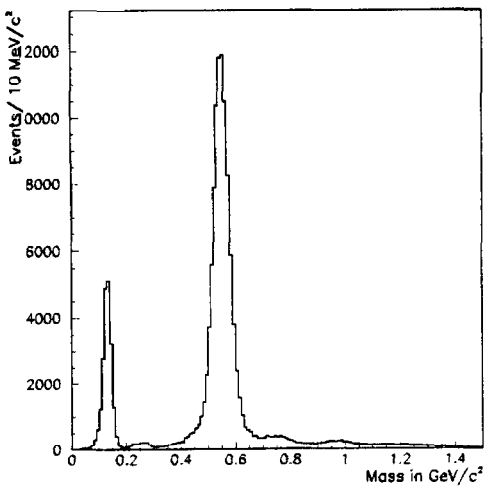

Fig. 7. The two photon effective mass (in GeV/c^2) with the trigger processor configured to select events with an effective mass greater than the mass of the π^0.

Since the algorithms discussed do not explicitly find clusters, the photon multiplicity cannot be evaluated exactly. However, a strong correlation exists between photon multiplicity and number of glass blocks over some threshold. In addition, if there are few clusters then, on average, each cluster has higher energy and therefore greater pulse height in fewer blocks. The trigger processor provides the maximum deposited energy in the LGD, and therefore additional information about the number of clusters.

In summary, the read-out controllers (ROCs) and trigger processor together deliver estimates of the total energy and the effective mass of photons hitting the LGD. They also give the number of modules above some energy and the maximum deposited energy. During experiment E852 the total energy trigger was used in conjunction with the *all-neutral event* trigger to select events with a majority of the beam energy in the lead glass detector. *Charged events* with a single π^0 were discriminated against by requiring a minimum effective mass in the LGD.

4. LGD tests

4.1. Magnetic shielding tests

Careful consideration was given to the fact that the LGD would be operating in the fringe field of the MPS magnet. Without the LGD and its magnetic shielding, the fringe field of the MPS was measured to be between 35 and 100 G at the LGD location. To shield magnetically the photomultipliers, the transporter was constructed of steel, the front of the glass stack was covered with a 0.5 in steel plate [14], and the photomultipliers and bases were held by the soft iron tubes of the cellular wall. Also, the photomultipliers were wrapped in 300 μm thick μ-metal shields.

Table 3
The fringe field measurements at LGD photomultiplier positions

Position of measurement	Main field (T)	Fringe field (G)
LGD 4 extreme corners	1.0	3.1 – 4.8
	0.0	0.7 – 1.5
LGD center	1.0	3.6 – 6.1
	0.0	0.7 – 1.5
Inside μ-metal shield	1.0	0.7
	0.0	0.1

Based on the relatively low field measurements (see Table 3, above) at the shielded positions of our PMTs, we chose to run without recessing the tubes in their soft iron and μ-metal shields. This greatly simplified the PMT mechanical mounting scheme. The results of tests of an optical coupling scheme with a thick cylindrical light guide are discussed in Ref. [4]. The decision to run without recessed photomultipliers lead to the consideration of the possible use of optical grease between PMTs and glass to reduce light loss at the boundary. Tests with and without optical grease are described in Section 4.4, below.

During the 1993 engineering run the 3045 element lead glass wall was installed along with the 0.5 in steel front plate and the darkroom. A prototype 81 element cellular wall with soft iron tubes and μ-metal was in place. Hall probe magnetic field measurements were made inside the darkroom at various positions around the glass stack and the prototype cellular wall. Table 3 summarizes the largest field components measured at different positions with the MPS magnet energized at full field (0.1 T) and with field off. These measurements indicate first that the transporter shielding was effective, and second that the field at the approximate position of the photocathodes of the LGD array was still not negligible (0.7 G). This fact influenced our calibration and monitoring strategies discussed in Section 5.

The ultimate decision to run without recessed tubes and with no optical grease was based on the π^0 mass resolution measured in the LGD. Tests carried out with and without field as well as tests with and without optical grease are discussed in Section 4.4.

4.2. Energy calibration with electrons

A 5 GeV negative beam was transported to the LGD. Existing beam line threshold Cherenkov counters tagged electrons in the beam and the LGD transporter system

was used to move each instrumented module into the beam. Data were collected and analyzed to obtain a preliminary measurement of the response of each module. The high voltages were adjusted so that each module gave a similar response and, the scan was repeated at these new voltages. The data collected were analyzed using the calibration algorithm described in Ref. [4] and calibration constants to convert photomultiplier pulse height to energy were obtained.

Fig. 8 shows the LGD reconstructed energy using the final values for the calibration constants minus the beam energy as determined by the MPS beam spectrometer. The energy resolution, as obtained from a Gaussian fit to the distribution is $\sigma/E = (5.13 \pm 0.07)\%$. The beam spectrometer contribution is small and is ignored in this comparison. Fig. 8 contains only events where the extrapolated electron was more than 10 cm from an edge of the instrumented area of the LGD.

4.3. LGD position resolution with electrons

Since charged particle tracking is available for electrons, the electron beam calibration scans described above are used to give a precision position measurement of the electron impact at the LGD. TDX4, a drift chamber with 180 μm resolution, is located immediately upstream of the LGD (see Fig. 1). The extrapolated charged track gives a 200 μm measurement of the electron position at the LGD. This error is sufficiently smaller than the errors expected from the LGD measurement of electron position (typically several mm) that it can be ignored in the determination of the LGD spatial resolution. Since the TDX4 chamber provides only x-coordinate information, this technique gives a direct measure of only the LGDs horizontal position resolution.

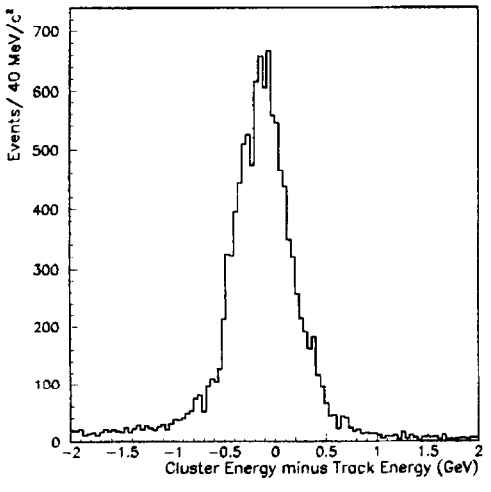

Fig. 8. The electron's deposited energy (in GeV) in the calibrated LGD minus the electron's energy (in GeV) measured by the beam spectrometer.

Neighboring blocks of deposited energy are clustered. The details of this clusterizing procedure are given in Section 5. Using the LGD energy deposition information, three methods for determining the beam electron's impact position are investigated. These are referred to below as the linear (LIN), the logarithmic (LOG) [15], and the modified logarithmic (LOG2) methods. In each case the position of the photon creating the electromagnetic shower is calculated using

$$x = \frac{\sum_{j=1}^{N} w_j(E_j) \cdot x_j}{\sum_{j=1}^{N} w_j(E_j)} \tag{11}$$

where E_j is the energy deposited in the jth module of the detector, x_j is the x-coordinate of the center of the jth module and the sum is carried out over all modules associated with the electron energy deposition cluster. The weights for each method are

$$w_j^{\mathrm{LIN}} = E_j, \tag{12}$$

$$w_j^{\mathrm{LOG,LOG2}} = \mathrm{Max}(0, a_0 + \ln E_j - \ln E_{\mathrm{tot}}), \tag{13}$$

where

$$a_0 = \frac{\ln E_{\mathrm{tot}}}{7} + 3.7 \tag{14}$$

and E_{tot} is the total energy of the cluster. The difference between the LOG and LOG2 methods is in how the weighting of the center block is handled. In the LOG2 method, the cluster seed module is de-weighted:

$$w'_{\mathrm{seed}} = w_{\mathrm{seed}} + (f - 1)(w_{\mathrm{seed}} - w_k), \tag{15}$$

where

$$f = \exp(-0.23 E_{\mathrm{tot}}). \tag{16}$$

Since the LGD is moving through the beam during the calibration, information from the position encoders is used to transform the extrapolated electron position into a coordinate system fixed on the center of the active area of the LGD. Fig. 9 shows the cluster positions modulo the glass block size for the three position finding techniques described above. The linear weighting shows a clear bias towards finding clusters centered near the center of modules. This bias is reduced for the LOG method, and almost completely eliminated for the LOG2 method. The sharp peak observed at the center for all three methods is due to clusters with small transverse dimensions.

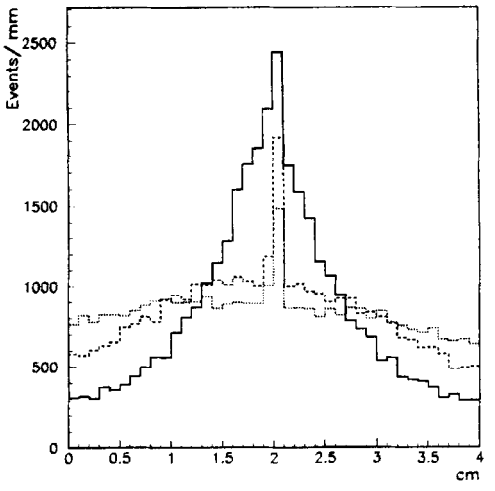

Fig. 9. Cluster positions (in cm) within a module for the three methods described in Section 4.3 below. LIN (solid line), LOG (dashed line), LOG2 (dotted line).

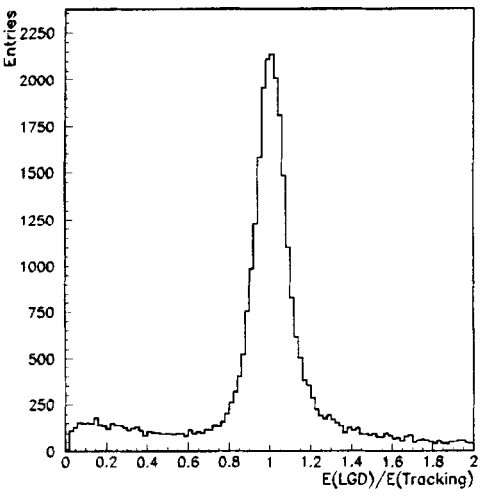

Fig. 10. The ratio E/p with the constraints described in the text.

4.4. LGD depth correction studies using electrons

When a photon strikes the LGD, the shower maximum occurs a distance D along its path in the glass called the shower depth. The shower depth is shown in Fig. 11. For a normally incident photon with a trajectory along the z-axis, the transverse (x,y) position of the photon's impact at the face of the glass corresponds to the (x,y) location of the shower maximum. However, for a photon entering the lead glass wall at an angle θ, this is no longer the case. A depth correction is needed. This depth correction for photons at an angle can be determined experimentally by observing showers from *electrons* hitting the lead glass wall at an angle.

Electrons are found in our standard hadron events both as a result of photon pair production and as a result of π^0 Dalitz decays. In both cases the opening angle between the electron-positron pair is small. This sample of electrons (and positrons) not only has a variety of entrance angles, but also has a spectrum of energies. This provides a mechanism to study the depth correction as a function of energy.

4.4.1. Electron selection

For charged tracks the ratio E/p is determined from the ratio of the LGD calorimeter energy to the spectrometer momentum. A plot of this ratio for electrons will show a peak at unity. We isolate a clean sample of electrons by starting with events with two oppositely charged tracks where one of the extrapolated charged tracks points close to an energy cluster in the LGD. Two additional requirements are imposed. First, the energy cluster must be narrow. (Energy deposition from hadrons tends to be broad.) Second, the opening angle between

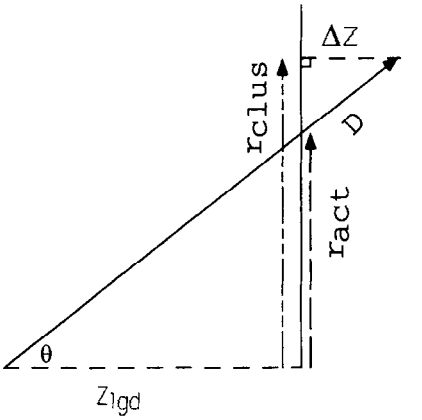

Fig. 11. The geometry of the shower depth D and the depth correction $r_{act} - r_{clus}$. The quantity z_{lgd} is the z distance from the event vertex to the face of the glass (about 5 m).

the two charged tracks in the event is constrained to be small ($\cos > 0.995$). Fig. 10 shows the clean electron (positron) peak from this selection procedure.

The geometric definition of the shower depth correction ($r_{clus} - r_{act}$) is also shown in Fig. 11. This correction is the difference in the (x,y) plane between the LGD cluster center and the actual impact position of the electron at the face of the glass. With the measured depth correction and the entrance angle, θ, of the electron, the shower depth is given by

$$\text{Depth} = D = \frac{r_{clus} - r_{act}}{\sin\theta}. \tag{17}$$

Selecting events with electrons at an angle of incidence greater than 8°, we calculate the depth of the shower in

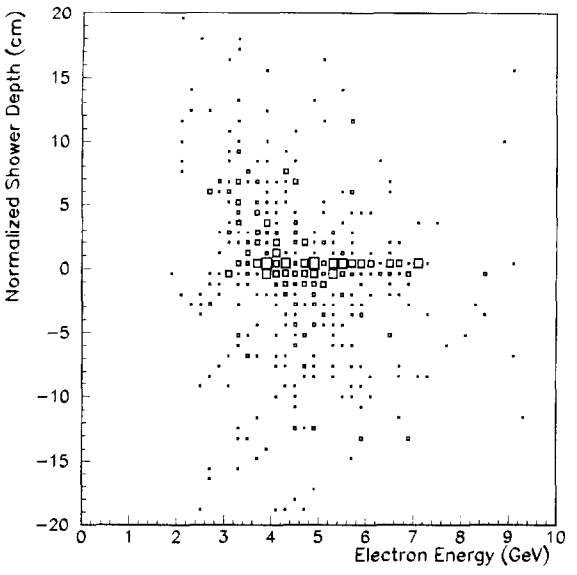

Fig. 12. Depth correction (in cm) versus track energy (in GeV).

the LGD. Fig. 12 shows the *normalized* shower depth ($D - 17.8$ cm) versus the energy of the electron and shows that the shower depth is, at best, a slow function of energy. Over this relatively narrow band of energies, the best average value of the shower depth, D is 17.8 cm of glass.

4.5. Optical coupling study

In the first of the prototype LGDs, described in Ref. [4], disks made of Sylgar™ were used to optically couple the lead glass to the photomultiplier. The thickness was such as to allow the photocathode to be located well inside the μ-metal shield. For the second prototype no optical coupling, other than an air gap, was employed. During the 1993 engineering run we sought to determine whether optical coupling, other than air, was needed. We first examined the effect of optical coupling on the energy resolution of the LGD. Second, we looked for a change in the mass resolution of π^0's.

4.5.1. Optical coupling test with 5 GeV electrons

During the 5 GeV calibration run with electrons, the MPS magnetic field was turned off, providing electrons at normal incidence to the glass. Two calibrations were performed, one with an air gap of order 1 mm between the lead glass and photomultipliers, and one with optical grease. For each condition the electron energy peak was calibrated to peak at 5 GeV, and a Gaussian fit done to give an estimate of the total energy resolution. The quantity σ/E was found to be 0.05 with and without optical grease. A significant increase in the number of photoelectrons collected would have decreased the statistical term in the shower energy resolution, narrowing the ratio σ/E. No such narrowing was observed.

4.5.2. Optical coupling test with pions

The influence of optical grease was also studied with 18 GeV incident π^- on a production target 5 m upstream of the LGD. Data were taken with and without optical coupling and with and without the 1.0 T MPS magnetic field. The event trigger selected all-neutral events with more than 12 GeV of energy in the LGD. A clear π^0 peak was observed in the di-photon effective mass distribution under all four running conditions. In each of the four cases, no measurable change in mass resolution was observed. The di-photon effective mass distribution is shown in Section 5 of this paper (Fig. 13) for the case of magnetic field and no grease. The mass resolution is 10.4 ± 0.1 MeV. This result is consistent with our measured electron calibration results showing no increase in σ/E with optical grease.

Based on these measurements, we chose not to use optical grease. Advantages of no optical coupler are several including ease of photomultiplier installation and replacement and improved long-term stability of the optics of the system.

5. LGD energy calibration from constrained fitting of events

In Section 4.2 we discussed the energy calibration of the LGD using an electron beam of known energy. Here we describe an energy calibration method utilizing photons from π^0's and η's in production data. A more detailed description of this calibration process is given in [16]. Throughout production data taking, this method was used to recalibrate the LGD for each set of runs taken between cyclings of the MPS magnetic field. These cyclings (turning the MPS magnet off and back on) were necessary for chamber repair or maintenance and did produce changes in the LGD energy calibration, thereby dividing the data taking into separately calibrated data sets (see also, Section 6.2). In this section we will describe the cluster finding, the conversion of clusters into photons, and the calibration algorithms themselves.

5.1. Cluster finding

The cluster finding algorithm first constructs a list of module energies and addresses in decreasing order in energy. The module with the largest energy is identified as a cluster center if its energy exceeds a first-level cluster seed threshold, E_1. After identifying all such first generation cluster centers and their neighboring blocks, a second level search looks for remaining blocks with energy

above a second level cluster seed threshold, E_2. Corresponding clusters of blocks are identified. Finally, the clusterizer shares energy in blocks within range of two identified centers.

5.2. Cluster seed thresholds and pedestals

The 1994 E852 data analysis was done with cluster seed thresholds set at $E_1 = 0.35\,\text{GeV}$ and $E_2 = 0.15\,\text{GeV}$. In order to reach these low thresholds, a detailed understanding of the ADC pedestals was required. The pedestals were measured at the beginning of each run. Occasional channels exhibited a wide pedestal variation with time. These pedestal fluctuations were occasionally large enough to generate spurious clusters. For example, at 0.007 GeV/count, a pedestal fluctuation of 22 ADC counts will generate a cluster seed. Thus, a pedestal width of 5 counts with a 4σ fluctuation, a common event with some three thousand channels, would be interpreted as a cluster. To reduce this effect and reap the benefits of lower energy cluster seeds, all clusters containing only one block were eliminated from the sample. The logarithmic weighting (LOG2 in Section 4.3), was used to find the position of each cluster.

5.3. Converting clusters to photons

At this point we extract each photon's energy and momentum from its cluster energy and position. The cluster position $\boldsymbol{r}_{\text{clus}}$ is determined using the LOG2 weighting discribed in Section 4.3. With the cluster depth D the actual photon position $\boldsymbol{r}_{\text{act}}$ is given by Eq. (17) in Section 4.4.1. For events without charged tracks in the final state, E852 cannot determine the exact position of the primary vertex. For these all-neutral data, the beam track is swum to the center of the target (in z), and this point ($\boldsymbol{r}_0$) is used as the primary vertex. The photon momentum is then given by

$$p = \frac{(\boldsymbol{r}_{\text{act}} - \boldsymbol{r}_0)}{|\boldsymbol{r}_{\text{act}} - \boldsymbol{r}_0|} E_{\text{c}}, \tag{18}$$

where E_{c} is the cluster energy.

5.4. Event selection for calibration

The calibration is performed on a sample of approximately 2 million normal events. After clusterizing, two, three, and four cluster events are selected for further analysis. Charged track and all-neutral events are handled differently. The calibration procedure used only the LGD information in the events. No attempt was made to remove energy deposited in the LGD by charged tracks. That is to say, there is no hadron rejection in the charged data, and other methods are used to clean up the sample.

Charged events (events with both charged tracks and photons in the LGD) are used as a source of π^0's with large transverse momentum. These wide angle π^0's illuminate all parts of the LGD. The two and three cluster events with π^0 candidates are selected. The π^0 window is defined to be a 1σ cut, where σ is defined by the width of the π^0 in the all-neutral two-cluster events. If a π^0 is found, it is fitted and passed to the calibration procedure. At this stage, before calibration, this σ is typically $30\,\text{MeV}/c^2$, compared to a width of $10.4\,\text{MeV}/c^2$ after calibration.

All-neutral events present a much cleaner sample, and a wider range of events are passed on to the calibrator. Two and three cluster events are searched for π^0's and η's, using simple window cuts. The π^0's are identified first, and if none is found, the η hypothesis is checked. The window cuts can be wider than in the charged analysis because the backgrounds are lower. The π^0 cut is 2σ, and the η cut is $5\sigma_{\pi^0}$ (The η width is a bit less than 3 times that of the π^0.) The four cluster sample is checked for $f_2 \to \pi^0\pi^0$. Here the π^0 window is again 2σ wide. The η's and π^0's are then fitted and passed on to the calibrator.

We found that a clean data sample was essential for calibration. Calibrations using samples with high backgrounds did not converge well. To reduce backgrounds, cuts were made on three parameters: the minimum cluster separation, the number of blocks in the event, and the energy of the lowest energy photon making up the massive parent. The cuts are summarized in Table 4.

5.5. Monitoring system corrections

A study of the monitoring system data has shown the system to be very stable (see Section 6 for more details). Run-by-run corrections based on the monitoring system remove a drift in the π^0 mass, seen over an extended period between magnet cycles. Two numbers are calculated for each run. The first is the average normalization tube output over the run, av_{norm}. The second is the

Table 4
Cuts used to select events for calibration

Sample	Minimum cluster separation (cm)	Min. # of blocks in event	Minumum photon energy (GeV)
Charged - 2 cluster	10	10	0.6
Charged - 3 cluster	11	14	0.6
Neutral - 2 cluster	8	18	None
Neutral - 3 cluster	8	14	0.6

average wall output, given by

$$\mathrm{av_{wall}} = \frac{\sum_{\text{events}} \left[\sum_{i=0}^{3045} s_i/3045 \right]}{\#\ \text{events}}.$$

The ratio $\mathrm{av_{wall}}/\mathrm{av_{norm}}$ is computed for each run, and the calibration constants for that run are scaled by the correction

$$\text{Correction} = \frac{\mathrm{ratio_{first\ run}}}{\mathrm{ratio_{current\ run}}}.$$

The correction is typically at the 1% level. The widths of the event-by-event distributions of the wall output and the normalization tube output track each other very well indicating that the widths are mainly due to variations in the laser output. The laser normalization tube, an RCA 8575, is located at the back of the darkroom, and has different systematics.

5.6. Two-photon constrained fitting

Before starting the calibration process the photons from a π^0 or η are fit to get an improved estimate of the energy of each photon. Full event fitting was not done in the calibration process for several reasons. Our full event fitter, SQUAW [20] is time consuming and requires a well contained event to function properly. By not requiring fully contained events in the calibrator, a larger data sample was introduced allowing better illumination of the detector. Also, if full event fitting were used, the charged data would have to be fully reconstructed before calibration could proceed [17].

The two-photon effective mass is given by

$$m^2 = (p_1 + p_2)^2 = 2E_1E_2 - 2\boldsymbol{p}_1 \cdot \boldsymbol{p}_2 = 2E_1E_2(1 - \cos\theta), \tag{19}$$

where p_1 and p_2 are the photon 4-momenta.

The χ^2 for the fit is given by

$$\chi^2 = \left(\frac{E_1' - E_1}{\sigma_1}\right)^2 + \left(\frac{E_2' - E_2}{\sigma_2}\right)^2, \tag{20}$$

where E_1 and E_2 are the fitted energies of the photons, E_1' and E_2' are the measured energies, and

$$\sigma_n = 0.02E_n' + 0.06\sqrt{E_n'} \tag{21}$$

is the energy resolution of the detector [19], where the E_n' are in GeV. We can rewrite the χ^2 in terms of E_1 only by using Eq. (19) for the fitted photons.

$$\chi^2 = \left(\frac{E_1' - E_1}{\sigma_1}\right)^2 + \left(\frac{E_2' - \dfrac{m^2}{E_1\ (1 - \cos\theta)}}{\sigma_2}\right)^2. \tag{22}$$

The fitting program, MINUIT [18] minimizes the χ^2 by adjusting both E_1 and θ.

5.7. The calibration process

The calibration process begins by setting all calibration constants to 7 MeV per ADC count. A first pass is made through the neutral events of the calibration data set, the π^0 peak is located and the calibration constants are scaled to put the π^0 at the correct mass. Complete passes are then made over the full charged and neutral data set, with new calibration constants determined after each pass. The width of the π^0 is determined from the neutral two cluster sample alone, and is fed back into the hypothesis sorting routines as described earlier. Good convergence is generally exhibited after 10–15 passes through the data.

5.7.1. Calibration results

Figs. 13 and 14 show the π^0 and η mass distributions from eight runs between two magnet cycles. The calibration constants for this set of runs was determined from data in only 2 of these runs. The remainder of the data uses calibration constants extrapolated from these runs using monitoring system corrections. The π^0 width is measured to be 10.4 ± 0.1MeV, and the η width is 25.1 ± 0.3 MeV. Fig. 15 shows the effect of the shower depth correction (see Section 5.3) to the total energy deposited in the glass. The depth correction brings photons closer together raising the corresponding energy of the η or π^0 and hence the total energy deposited in the glass.

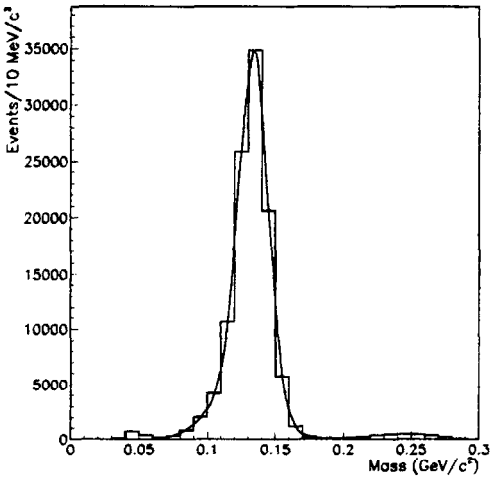

Fig. 13. All-neutral two photon mass distribution (in GeV/c^2) in π^0 region. The fit is to a double Gaussian and is discussed in Section 5.7.1.

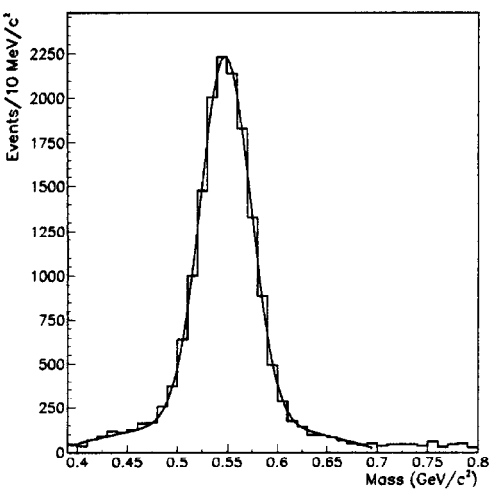

Fig. 14. All-neutral two photon mass distribution (in GeV/c^2) in η region. The fit is to a double Gaussian. Note that the position of the η mass is very sensitive to a good background fit.

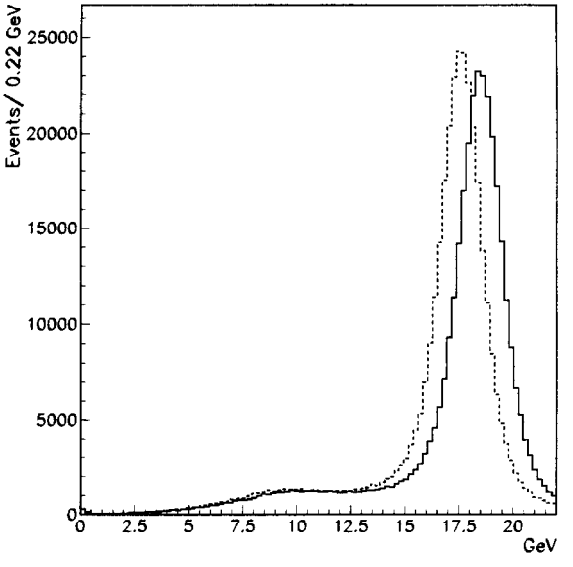

Fig. 15. Total energy (in GeV) in the glass, all-neutral events. The dashed line is without the depth correction to the photon position; the solid line includes the depth correction.

6. LGD monitoring system

6.1. Monitoring system response

The monitoring system described in Section 2.5 distributes light to each module utilizing a laser system feeding a set of three large cast acrylic sheets. A monitor event is taken at the end of each beam spill during all production data taking. This system provides information about both the spatial and temporal variations of individual modules in the lead glass wall.

While the acrylic sheets distribute the laser light fairly uniformly to all lead glass blocks, nonuniform spots are found at the two interfaces between the sheets and at several of the eighteen fiber inputs. Tilting of the light fiber inputs toward the front or back of a acrylic sheet will, for example, produce nonuniform illumination. Uncalibrated lead glass blocks are also visible in a two-dimensional plot of these monitoring system events. Ignoring the fiber input regions and seams between acrylic sheets, the variation of light across the LGD is at the $15 \pm 10\%$ level. This spatial variation was small enough to allow us to use the monitoring system for preliminary gain setting without beam. However, we chose to set preliminary gains using previously measured gain versus high voltage characteristics of each tube.

As a function of *time*, the monitoring system proved to be quite stable. As described in Section 5.5, the average wall response was calculated by averaging all ADC modules for each pulse of the laser, and then normalizing this average by the response of the laser. Between cyclings of the MPS magnet, the standard deviation in the average wall response was measured to be 0.7%. The laser light output itself had a single pulse standard deviation of 0.4%.

In addition to the calibration corrections described in Section 5.5, this temporal stability of the monitoring system was utilized at several levels in setting up and monitoring the experiment. For example, channels with abnormal monitoring signals flagged problematic bases and tubes during data taking. In addition, we set the voltage level of newly replaced base-tube assemblies by using the constant light level of the monitoring system. The monitoring system was also a useful diagnostic tool during the cabling and electronic checkout of the lead-glass wall.

6.2. Monitoring system implementation

Because the monitoring system could detect fluctuations in the detector at less than the 1% level, it became useful in providing information about average changes in the response of the LGD throughout the data-taking runs. It was extensively used on-line to provide important alarms related to the photomultiplier high voltage system, for example.

During a several month run, the MPS magnet was turned off and back on for chamber repair and maintenance a number of times. This cycling of the magnet changed the average signal in the LGD detector, sometimes substantially. This was most likely due to field hysteresis in the magnetic shielding and the corresponding change in gain of the photomultipliers, all of which were subject to the fringe field of the MPS magnet. Between these cyclings of the MPS magnet, on the other

hand, the LGD functioned stably. Variation in the average wall response was 0.7% from run to run, between magnet cycles. As mentioned in Section 5.5, we used the average wall response on a run by run basis to make a small overall scale correction to the calibration, for runs taken between cycles of the MPS magnet. Across magnet cycles, however, the monitoring system was unable to provide reliable corrections to the calibration constants. We were obliged to recalibrate the LGD, using the constraints on photons from π^0's and η's as described in detail in Section 5.

7. Performance of the LGD

From the analysis of approximately 25% of the 10^9 physics triggers taken in the 1994 and 1995 runs of experiment E852, we give a number of bench marks of the performance of the lead-glass detector.

7.1. All-neutral mass distributions

As discussed earlier in this paper, the widths of reconstructed resonances such as the $\pi^0 \to \gamma\gamma$, and $\eta \to \gamma\gamma$ provide measures of the combined position and energy resolution of the LGD. Table 5 summarizes these results and adds results from other topologies discussed below. All resonances except the π^0 and η have been fitted using SQUAW [20].

The two-photon all neutral events are made up largely of π^0 and η charge exchange events where the π^0 and η have energies near the beam energy. A stringent test of the calibration of the LGD over a wider energy range is provided by combined mass distributions from events with higher photon multiplicities. Fig. 16 shows a $\pi^0\pi^0$ mass plot from events with 4 photons in the LGD. The measured mass and width of the prominent $f_2(1270)$ are 1278.7 ± 1.8 and 178.8 ± 4.5 MeV. This can be compared with the Particle Data Group [21] mass of 1275 ± 5 MeV and width of 185 ± 20 MeV. Similarly, an $\eta\pi^0$ mass plot from events with 4 photons shows strong

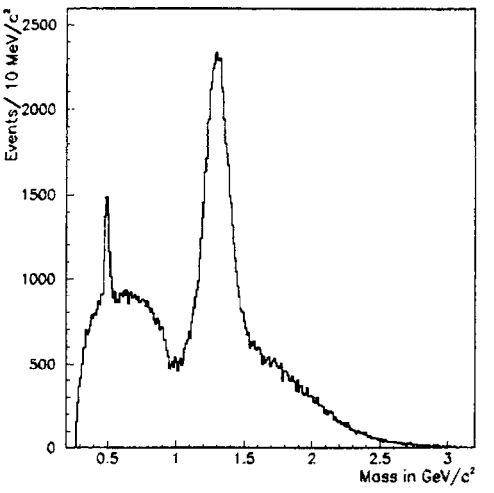

Fig. 16. $\pi^0\pi^0$ mass distribution (in GeV/c^2) from four-photon events.

$a_2(1320)$ and $a_0(980)$ resonances with resonant parameters given in Table 5.

Fig. 17 is taken from six-photon events. The prominent peak is the η decaying to $3\pi^0$'s. The full width of this peak is 28.3 MeV

7.2. Combining the LGD with charged tracks

Essential to experiment E852 is the extension of the search for exotics, hybrids, and glueballs into the realm of particle decays into both charged and neutral particles. Illustrating the power of the combined system, Figs. 18 and 19 show the effective mass of the $\eta' \to \eta\pi^+\pi^-$ system.

In Figs. 18 and 19 the η' is seen to lie on very little background. A fit to its mass gives 959.3 ± 0.2 MeV to be compared with the PDG [21] value of 957.77 ± 0.14 MeV for the η' mass. The experimental width (σ) is 6.4 MeV. Our experimental width of the η' is considerably smaller than the corresponding width of the

Table 5
Masses and widths of well-known resonances observed by E852 in all-neutral decay modes

Decay	E852		PDG [21]	
	Mass (MeV)	Width (MeV)	Mass (MeV)	Width (MeV)
$\pi^0 \to \gamma\gamma$	134.0 ± 0.1	10.4 ± 0.1	134.9	0
$\eta \to \gamma\gamma$	548.1 ± 0.3	25.1 ± 0.3	547.5	0
$f_2(1270) \to \pi^0\pi^0$	1278.7 ± 1.8	178.8 ± 4.5	1275 ± 5	185 ± 20
$a_2(1320) \to \eta\pi$	1314 ± 2	129 ± 6	1318.5 ± 1.6	103.4 ± 2.1
$a_0(980) \to \eta\pi^0$	989.6 ± 2.6	75.7 ± 10.7	982.4 ± 1.4	57 ± 11

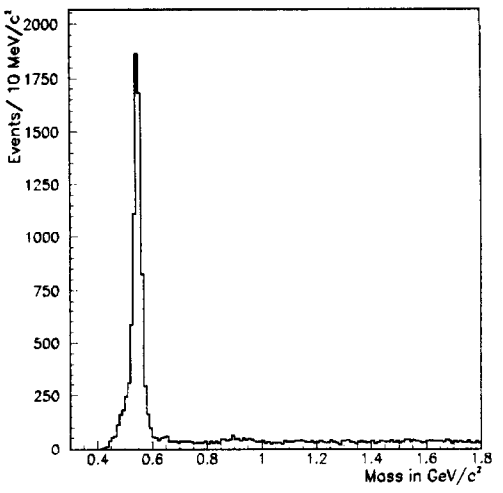

Fig. 17. $3\pi^0$ mass distribution (in GeV/c^2) from six-photon events.

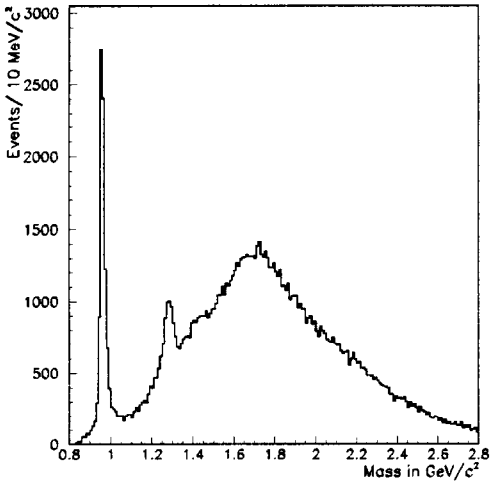

Fig. 18. The observed $\eta\pi^+\pi^-$ effective mass distribution (in GeV/c^2).

η' decaying to all neutrals through two photons or through $\eta\pi^0\pi^0$ because the charged tracks in the decay localize the decay vertex.

8. Summary

We have described the design, construction, and testing and of a 3045-element lead glass detector used in the Brookhaven AGS experiment E852. Our analysis includes both all-neutral events and events with charged tracks. In both cases the lead glass detector provided precision data on photons from a wide variety of hadron decays. Key to the success of the detector was its ability to provide triggers based on the characteristics of the photon distributions in the lead glass.

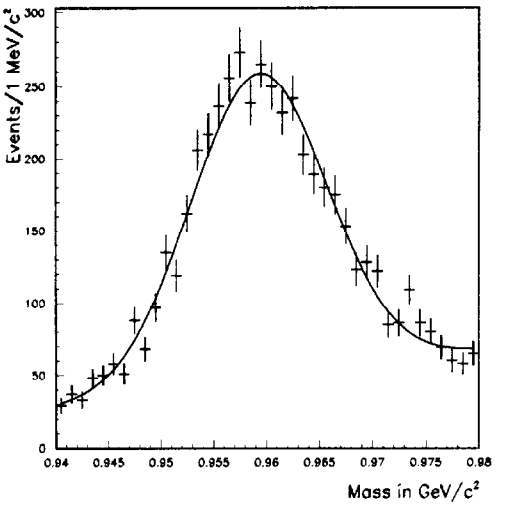

Fig. 19. The $\eta\pi^+\pi^-$ effective mass region near the η' (in GeV/c^2).

Acknowledgements

We are deeply grateful both to the staffs of the participating institutions and to the staff of the Alternating Gradient Synchrotron at Brookhaven National Laboratory. Their contributions to this work were invaluable. In the US, this work was supported in part by DoE grants at Indiana University, the University of Notre Dame, and Northwestern University, by NSF grants at the University of Massachusetts Dartmouth, the University of Notre Dame, and Rensselaer Polytechnic Institute. In Russia, this work was supported in part by the Ministry of Science, Highest School and Technical Policy of Russian Federation and the USSR State Committee for Utilization of Atomic Energy.

References

[1] E. Platner, IEEE Trans. Nucl. Sci. NS-25 (1978) 35;
A. Etkin, IEEE Trans. Nucl. Sci. NS-26 (1979) 54;
A. Etkin and M. Kramer, IEEE Trans. Nucl. Sci. NS-27 (1980) 139;
A. Etkin et al., Phys. Rev. D 22 (1980) 42;
S. Eiseman et al., IEEE Trans. Nucl. Sci. NS-30 (1983) 149;
S. Eiseman, Nucl. Instr. and Meth. 217 (1983) 140;
M.G. Rath et al., Phys. Rev. D 40 (1989) 693.
[2] T. Adams et al., Nucl. Instr. and Meth. A 368 (1996) 617.
[3] Z. Bar-Yam et al., Nucl. Instr. and Meth. A 386 (1997) 235.

[4] B.B. Brabson et al., Nucl. Instr. and Meth. A 332 (1993) 419.
[5] F. Binon et al., Nucl. Instr. and Meth. A 248 (1986) 89; J.R. Patterson, Ph.D. Thesis, University of Chicago, 1990, and additional references given in Ref. [4].
[6] S. Teige, Calorimetry in High Energy Physics, Brookhaven National Laboratory, 25 September–1 October, eds. Gordon and Rueger (World Scientific, 1994) p. 161.
[7] The Cockcroft-Walton voltage multiplier bases were designed and built at Moscow State University. The base design is discussed in detail in Ref. [4].
[8] The epoxy was chosen to have a low (3000 cP) mix viscosity. It was manufactured under the trade name Insulcast 125 Insulcure 20 by Permagile Industries, Inc., Plainview, New York, 11803.
[9] Goretube, Inc., 2300 South Calhoun Rd., New Berlin, WI 53151.
[10] Undergraduates B. Kern and Z. Ziliak developed a cabling algorithm to minimizing the ADC read-out time of 3045 channels into 4 FASTBUS crates.
[11] Laser Photonics, LN-300C nitrogen laser.
[12] Auburn Plastic II-UVA, military specification, pre-shrunk, guaranteed optically clear, index of refraction 1.49, and thickness (1.27 + 0.076/-0.178) cm.
[13] The high current BiRa model 8189-5 FASTBUS power supply provides + 5 V @ 300 A, − 5.2 V @ 300 A, − 2 V @ 200 A, + 15 V @ 100 A, and − 15 V @ 100 A.
[14] The influence of radiator just in front of the lead glass wall was studied using an electron beam and was reported on in Ref. [4]. The 0.5 in of steel corresponding to 1.7 radiation lengths of steel was found to increase the energy measuring error from 0.121 ± 0.005 to 0.133 ± 0.005 GeV for 3 GeV electrons, for example.
[15] T.C. Awes et al., Nucl. Instr. and Meth. A 311 (1992) 130.
[16] R. Lindenbusch, An Analysis of $\pi^- p \to \eta\pi^0 n$ at 18 GeV/c, Ph.D. Thesis, Indiana University, July 1996.
[17] In the analysis of the later 1995 data set, full charged particle event reconstruction was completed before LGD calibration began. Background from hadronic showers was identified before calibration. This both enhances the illumination of the calorimeter during calibration and reduces backgrounds leaking into the calibration process.
[18] MINUIT, Function Minimization and Error Analysis Program, CERN-CN Division, ASD Group – Users Guide to Program Library, D506, CERN, 1993.
[19] The energy resolution function for this photomultiplier-lead glass combination was determined from prototype measurements, and is discussed in Ref. [4]. The energy dependence of the resolution function follows the form $\sigma/E = (a + b/\sqrt{E})\%$, and was found to be independent of incident angle for the relevant angular range from 0° to 18°.
[20] SQUAW A kinematic fitting program, Programming Notes, University of Maryland, T. Day, Technical Report # 649.
[21] L. Montanet et al., Review of Particle Properties, Phys. Rev. D 50 (1994) 1173.